Towards the electronic structure of the NiMnSb / InP {100} interface: A density-functional approach
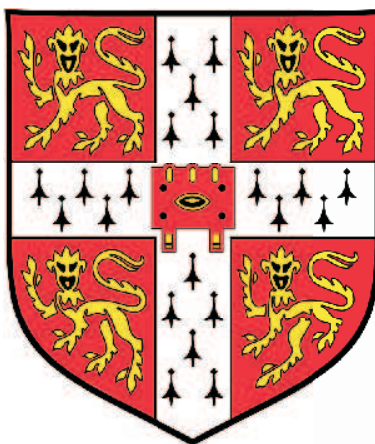
Joe Kwiatkowski

Part III Project

Declaration

This dissertation is submitted in partial fulfilment of the requirements for Part III Chemistry. It describes the work carried out in the Department of Chemistry in the Michaelmas Term 2004 and the Lent Term 2005. Unless otherwise indicated, the research described is my own and not the product of collaboration.

Signed

Joe Kwiatkowski

Acknowledgements

I would like to thank the people who suffered the painful ignorance of a Part III student. Thanks particularly to Steve Jenkins for his time and supervision and Zhi-pan for the DFT discussions and some beautiful pseudopotentials.

Contents

Part I

Introduction

1.1 Half-metals and Spintronics

In 1983 a new class of materials, the half-metals, was predicted in which electrons at the Fermi level are fully spin polarised (1). An example of this is the band structure of NiMnSb shown in figure 1. Bands of the majority spin state cross the Fermi level whilst those of the minority spin do not. The remarkable consequence of this is that NiMnSb conducts majority-spin electrons while acting as a semiconductor to minority-spin electrons - hence the name 'half-metal'. Very few materials display
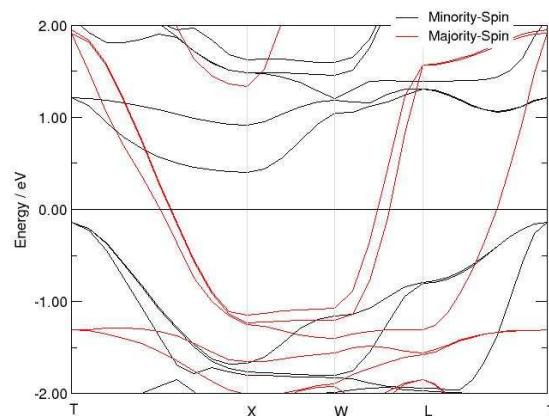
Figure 1: Majority and minority band structures of NiMnSb showing 100% polarisation of density of states at the Fermi-level

half-metallic behaviour although some notable examples are CrO_2 (2), NiMnSb (1) and similar structures such as PtMnSb (3).

Interest in half-metals has long been associated with the rapidly developing field of spin-electronics (spintronics). Spintronics exploits the spin of an electron in controlling its flow through some device (4). One of the many advantages that such devices have over those of conventional electronics is that magnetic rather than electric fields can be used to determine electron movement, and this can dramatically reduce switching times. Current spintronic devices include non-volatile random access memory and disk-drive technology. Future applications could include quantum

computing and novel logic circuitry. Intricate to the working of a spintronic device is the ability to produce and respond to a spin-polarised current. The complete spin polarisation of half-metals at the Fermi level therefore makes them potentially very useful to the spintronics industry.

A spintronic device that could be vastly improved by the use of half-metals is the spin-valve. Crude spin-valves already exist, and an example of their use is the hard-drive technology first introduced by IBM in 1997. The spin valve they employed (figure 2) consists of two ferromagentic materials, one pinned in a certain magnetic orientation and the other free. Because ferromagnets display a degree of spin polarisation at the Fermi level, a current flowing out of the free layer and into the pinned layer will also be spin polarised. If both layers are magnetically aligned then there will be better conduction than when the layers are anti-aligned. The change in resistance between the two cases (of about 8% in working devices) can be used to determine the magnetic environment experienced by the free layer and in this fashion data can be read from a spinning hard drive. The excitement surrounding half-metals is that if the ferromagnetic layers could be replaced by half-metals (figure 4), then in principle a change in resistivity of 100% could be realised. This huge response would allow magnetic domains to be made smaller and spun faster, enabling greater data storage densities and faster access speeds.

1.2   Half-metal / Semiconductor interfaces

Spintronic devices require the injection of spin polarised currents across interfaces, particularly those interfaces made with semiconductors. At an interface formed by a half-metal the loss of translational symmetry may sufficiently disrupt the band structure to destroy the Fermi level spin polarisation. This means that on crossing this interface, a spin polarised current would loose its coherence due to spin flip scattering. This consideration is one major problem preventing the widespread use of half-metals in spintronic applications and for this reason it is necessary to study the interfaces made by half-metals.

A particularly relevant interface is that made between NiMnSb and the semiconductor InP. NiMnSb is the prototypical half-metal with a large body of experimental (5) and theoretical (6; 1) work documenting its properties and it also has a high
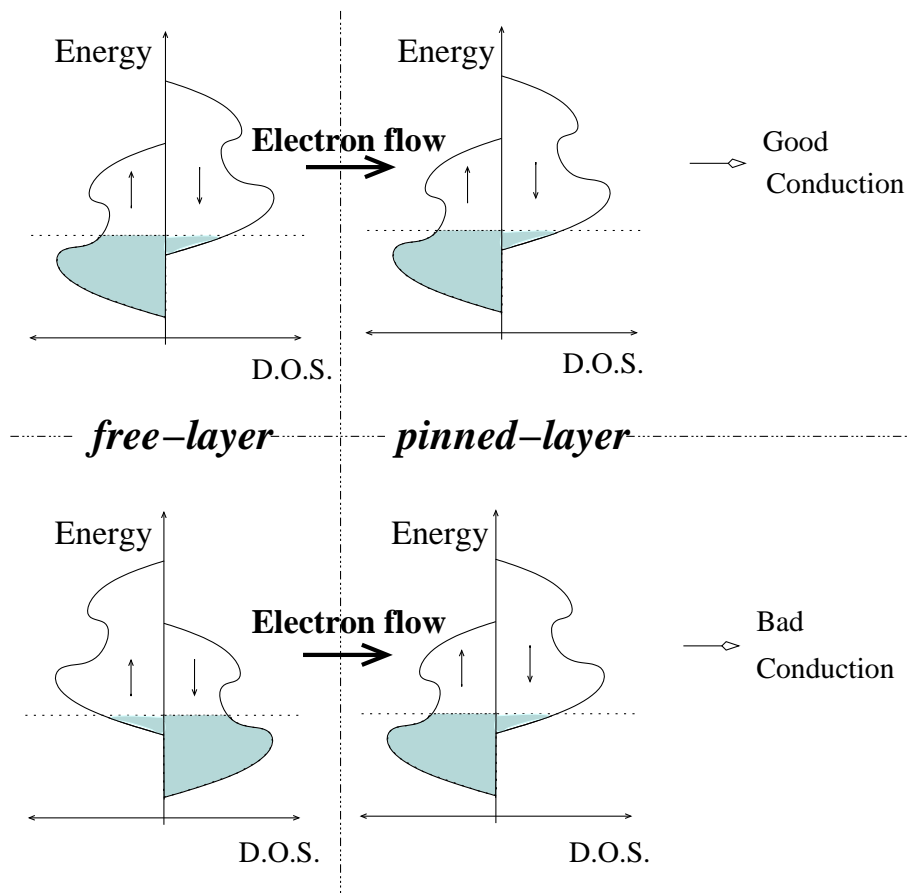
Figure 2: *A sketch of density of states (DOS) against energy.* A crude spin-valve of two ferromagnetic layers, one pinned and one free. The density of states at the Fermi-level is greater for the majority spin species and therefore aligned ferromagnets conduct better than when anti-aligned.

curie temperature of 760 K (7). InP is commonly used in the opto-electronic industry and has a lattice constant which differs to that of NiMnSb by only 1%. This means that at the interface there will be minimal distortion from bulk geometries and this is very convenient for modelling. Specifically, the {100} interface is chosen because the {100} surface is the only NiMnSb surface that can be experimentally characterised with any degree of certainty (8).

This thesis presents work towards an understanding of the interface between NiMnSb and InP by use of density-functional theory. It has been claimed in previous theoretical studies that the NiMnSb / InP {100} interface is not half-metallic (9). However, this work uses a very crude model where two materials are simply joined in their bulk geometries and the interface subsequently relaxed. It may be that a more accurate description of the interface yields a different interface structure that retains the half-metallicy of bulk NiMnSb.
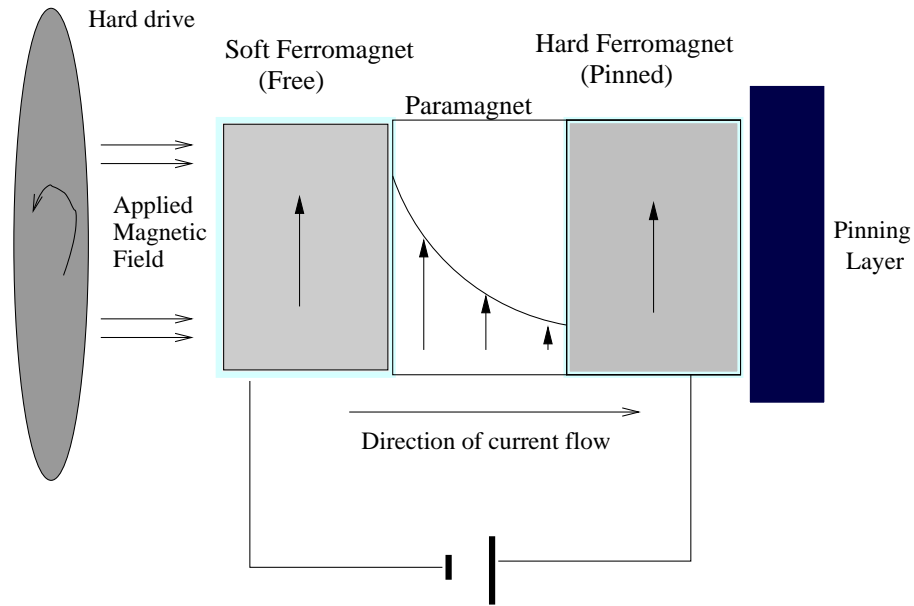
Figure 3: The use of a spin-valve in hard drive technology. The free layer aligns with the magnetic domain directly underneath it. By measuring the resistivity of the spin-valve, the state of the magnetic domain can be read.
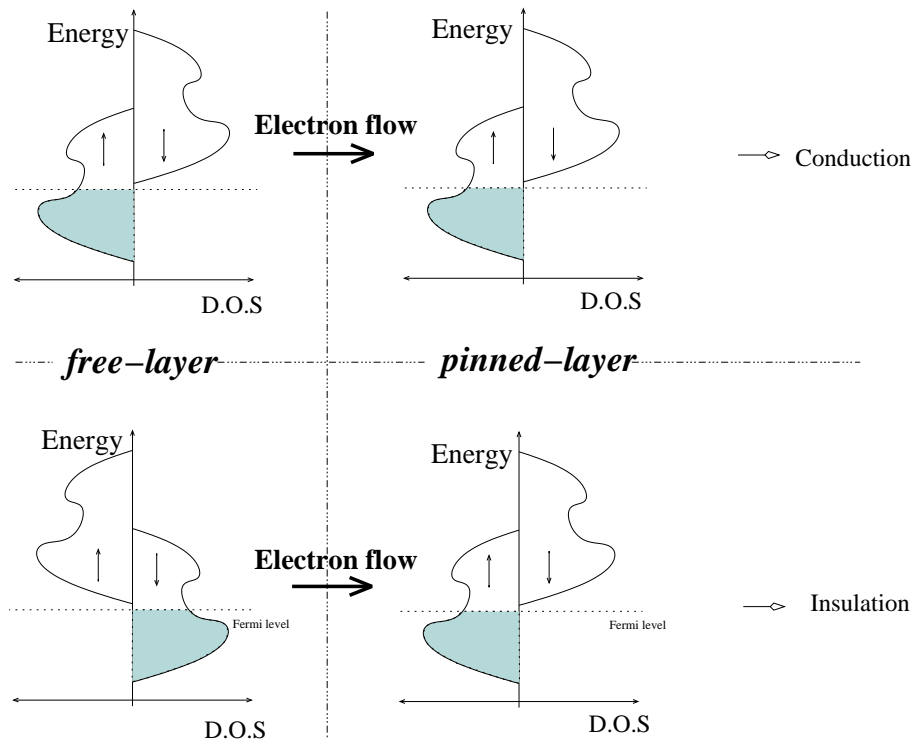
Figure 4: *A sketch of density of states (DOS) against energy.* An ideal half-metal spin-valve with 100% change in resistivity.

In constructing a more accurate model, the optimum geometry of the InP{100} surface is found and then NiMnSb is built onto this, layer by layer. At every stage of this process the structure is allowed to relax to its optimum state. In this thesis a model for the InP{100} surface is developed in preparation for further work on

the NiMnSb / InP {100} interface.

Part II

Theory and Methodology

2 Density Functional Theory

The beginnings of density-functional theory are in the papers of Thomas and Fermi in the 1920s, but only during the 1960s in the work of Kohn Sham and Hohenberg (10; 11) did the theory become complete and accurate. Over the 1990s density-functional theory took centre stage in computational chemistry and it is now the method of choice for a huge range of calculations because of its excellent accuracy and computational economy.

The essence of density-functional theory is to redefine the many-body problem of interacting electrons in the form of a single particle moving in an effective local potential. Although the form of this potential is unknown, and likely to remain forever unknown, significant ground can be covered by making approximations to it. The only justification for using these approximations is the quality of results that it produces. As such, density-functional theory is limited to only ever being semi-empirical in nature. A full derivation and discussion of a working theory can be found in (12; 13). The key steps are summarised below.

2.1 The Hohenberg-Kohn Theorems

The Hohenberg-Kohn theorems form the basis of density-functional theory by relating the energy of a system to its electron density. There are two theorems, or more exactly a single theorem and a corollary.

Firstly, the Hamiltonian is written within the Born-Oppenheimer approximation in terms of the electron kinetic energy T, the electron-electron interaction term V_{ee} and the external potential V_{ext},

$$H = T + V_{ee} + V_{ext} = F + V_{ext} \qquad ^{\text{a}} \tag{1}$$

where $F = T + V_{ee}$ and $V_{ext} = \int d\mathbf{r}\, \rho(\mathbf{r}) v_{ext}(\mathbf{r})$. Note that all ground state properties of the system are dependent on only the external potential V_{ext}, and the number

of electrons N. That the form of F is independent of both makes it universal for all systems and this fact greatly contributes to the wide applicability of density-functional theory. The first theorem states,

Theorem 1 *There is a one-to-one correspondence between the ground-state electron density of an N-electron system and the external potential acting upon it.*

This is proved by contradiction. Assume there are two potentials $v_1(\mathbf{r})$ and $v_2(\mathbf{r})$ with associated Hamiltonians $\hat{H}_1$ and $\hat{H}_2$ and ground state wave functions ψ_1 and ψ_2 with energies E_1 and E_2. If v_1 and v_2 result in the same ground state density $\rho(\mathbf{r})$ then by the variational principle

$$E_1 = \langle\psi_1|\hat{H}_1|\psi_1\rangle \leq \langle\psi_2|\hat{H}_1|\psi_2\rangle = \langle\psi_2|\hat{H}_2|\psi_2\rangle - \langle\psi_2|(\hat{H}_1 - \hat{H}_2)|\psi_2\rangle \tag{2}$$

so

$$E_1 \leq E_2 + \int d\mathbf{r}\, \rho(\mathbf{r})\left[v_1(\mathbf{r}) - v_2(\mathbf{r})\right] \tag{3}$$

Running the argument in the reverse order gives

$$E_2 \leq E_1 + \int d\mathbf{r}\, \rho(\mathbf{r})\left[v_2(\mathbf{r}) - v_1(\mathbf{r})\right] \tag{4}$$

which contradicts equation 3 unless $v_1 = v_2$.

That the density ρ determines v_{ext} means it must also define all ground state properties including the wave function (since ρ also trivially defines the number of electrons N). Thus the ground state energy and all its contributing terms can be written as functionals of ρ,

$$E[\rho] = T[\rho] + V_{ee}[\rho] + V_{ext}[\rho] = F[\rho] + \int d\mathbf{r}\rho(\mathbf{r})v_{ext}(\mathbf{r}) \tag{5}$$

This is the very heart of density functional theory; the highly dimensional wave function has been replaced by the far simpler electron density. Of course, the simplification to three dimensions means having to guess the form of the very complicated functionals of equation 5. This is discussed further in section 2.3.

All practical calculations depend on the second Hohenberg-Kohn theorem, often called the density-functional theorem,

Theorem 2 *For a trial density $\tilde{\rho}(\mathbf{r})$ such that $\tilde{\rho}(\mathbf{r}) \leq 0$ and $\int d\mathbf{r}\tilde{\rho}(\mathbf{r}) = N$,*
$$E_0[\rho] \leq E[\tilde{\rho}]$$

where $E_0[\rho]$ is the exact ground state energy produced by the exact density ρ. This follows immediately from the first theorem which showed that a density $\tilde{\rho}$ must determine its own ground state wave function $\tilde{\Psi}$. Thus the minimisation of the energy with respect to the density ρ is equivalent to the normal variational minimisation with regard to the wave function. Thus, assuming we have a good functional representation for $E[\rho]$, we can find the equilibrium configuration of a system by minimisation of the total energy with respect to the density. This must be done subject to the constraint

$$\int d\mathbf{r}\, \rho(\mathbf{r}) = N \tag{6}$$

and so we introduce the Lagrange multiplier μ [b] and find the stationary points of the expression

$$\frac{\delta}{\delta\rho(\mathbf{r})}\left\{ E[\rho] - \mu\left[\int d\mathbf{r}\, \rho(\mathbf{r}) - N\right] \right\} = 0 \tag{7}$$

which, by the calculus of variations, gives the Euler-Lagrange equation

$$\mu = \frac{\delta E[\rho]}{\delta\rho(\mathbf{r})} = v_{ext}(\mathbf{r}) + \frac{\delta F[\rho]}{\delta\rho(\mathbf{r})} \tag{8}$$

This equation is exact, but the form of $F[\rho]$ remains unknown. In the treatment by Kohn and Sham this difficulty is dealt with such that the variational method can be pursued.

2.2 The Kohn-Sham equations

Kohn and Sham choose first to represent the electron density ρ by a set of wholly fictitious non-interacting single electron orbitals,[c]

$$\rho(\mathbf{r}) = \sum_i^N |\psi_i(\mathbf{r})|^2 \tag{9}$$

where the ψ_i are necessarily orthonormal. Secondly, they split $F[\rho]$ into three parts,

$$F[\rho] = T_s[\rho] + J[\rho] + E_{xc}[\rho] \tag{10}$$

---

[b]From equation 7 it is evident that μ is the change in energy with respect to change in the number of electrons - i.e. the chemical potential.

[c]It may seem counterintuitive that we re-introduce wave functions after working so hard to dispense with them and their complexity. However, this considerable loss of simplicity is worth sacrificing for the excellent method of treating the kinetic energy that it allows.

where T_s is the kinetic energy of the non-interacting orbitals

$$T_s = \sum_i^N \left\langle \psi_i \middle| -\frac{1}{2}\nabla^2 \middle| \psi_i \right\rangle \tag{11}$$

and $J[\rho]$ is the classical coulomb repulsion part of V_{ee}

$$J[\rho] = \iint d\mathbf{r_1}\, d\mathbf{r_2}\, \frac{\rho(\mathbf{r_1})\rho(\mathbf{r_2})}{|\mathbf{r_1} - \mathbf{r_2}|} \tag{12}$$

and the exchange-correlation energy $E_{xc}[\rho]$ is defined to contain everything else necessary to make equation 10 an equality,

$$E_{xc} \equiv T[\rho] - T_s[\rho] + V_{ee}[\rho] - J[\rho] \tag{13}$$

As a result of this very clever formulation, only E_{xc} is unknown. Moreover E_{xc} is presumably small, being only the nonclassical part of $V_{ee}[\rho]$ and the difference between T and T_s.[d] The Euler-Lagrange equation (equation 8) now becomes

$$\mu = v_{eff}(\mathbf{r}) + \frac{\delta T_s[\rho]}{\delta\rho(\mathbf{r})} \tag{14}$$

where the v_{eff} is the Kohn-Sham effective potential

$$v_{eff}(\mathbf{r}) = v_{ext}(\mathbf{r}) + \frac{\delta J[\rho]}{\delta\rho(\mathbf{r})} + \frac{\delta E_{xc}[\rho]}{\delta\rho(\mathbf{r})} = v_{ext}(\mathbf{r}) + \int d\mathbf{r_2}\, \frac{\rho(\mathbf{r_2})}{|\mathbf{r_1} - \mathbf{r_2}|} + v_{xc}(\mathbf{r}) \tag{15}$$

where v_{xc} is the exchange-correlation potential, given by

$$v_{xc}(\mathbf{r}) = \frac{\delta E_{xc}[\rho]}{\delta\rho(\mathbf{r})} \tag{16}$$

Equation 14 is exactly the result that would be derived for a system of electrons that were genuinely noninteracting and moving in an external potential v_{eff}. Therefore, simply solving the N one-electron equations

$$\left[-\frac{1}{2}\nabla^2 + v_{eff}(\mathbf{r}) \right] \psi_i = \epsilon_i \psi_i \tag{17}$$

gives the density $\rho(\mathbf{r})$ from equation 9. Equations 17 are the much celebrated Kohn-Sham equations.[e] These equations are exact in principle, and yet they are simpler than the Hartree-Fock equations because $v_{eff}(\mathbf{r})$ is a local potential, depending only on $\mathbf{r}$ at a single point in space. However, the value at this point is dependent upon

---

[d]E_{xc} also contains a correction for the unphysical interaction of an electron with itself that results from the definition of the coulomb potential, $J[\rho]$. This does not occur in regular quantum chemistry where the self-interaction terms of the exchange and coulomb terms cancel.

[e]Alternatively the Kohn-Sham equations may be derived by minimising the total energy with the standard variational procedure on the orbitals ψ_i, subject to the constraint $\int d\mathbf{r}\, \rho(\mathbf{r}) = N$.

ρ (equation 15) over all space (in some difficult and inaccessible way) and so these equations must be solved iteratively until self-consistency is achieved. When this criteria is met the energy can be computed directly from either

$$E[\rho] = \int d\mathbf{r}\, \rho(\mathbf{r})v_{ext}(\mathbf{r}) + T_s[\rho] + J[\rho] + E_{xc}[\rho] \tag{18}$$

or

$$E = \sum_i^N \epsilon_i - \frac{1}{2} \int d\mathbf{r_1} d\mathbf{r_2}\, \frac{\rho(\mathbf{r_1})\rho(\mathbf{r_1})}{|\mathbf{r_1} - \mathbf{r_2}|} + E_{xc}[\rho] - \int d\mathbf{r}\, v_{xc}(\mathbf{r})\rho(\mathbf{r}) \tag{19}$$

2.3 The Exchange-correlation functional

The Kohn-Sham formalism allows an exact treatment for the majority of the electronic energy, with all the remaining unknowns collected into the exchange correlation functional E_{xc} (equation 13). The accuracy of this approach depends entirely on the quality of the chosen approximation to E_{xc}, but there exists no systematic way to improve upon this. The only exception is the uniform electron gas for which contributions to the exchange correlation energy can be considered accurately.

2.3.1 The Uniform electron gas and Local density approximation

In the uniform electron gas a uniform spread of positive charge neutralises N electrons which are delocalised over a volume V where $N \to \infty$ and $V \to \infty$ with the electron density ρ remaining finite. Within such a model the total energy depends only on the kinetic energy T_s and the exchange-correlation energy E_{xc}.[f] Moreover E_{xc} can be split into an exchange and a correlation term E_x and E_c

$$E[\rho] = T_s[\rho] + E_{xc}[\rho] = T_s[\rho] + E_x[\rho] + E_c[\rho] \tag{20}$$

Of these, it is possible to derive analytically the kinetic energy T_s and the exchange energy E_x. There is no explicit expression known for E_c, but it can be determined numerically by subtracting T_s and E_x from the total energy calculated by quantum Monte Carlo simulations. Analytic forms for E_c have been suggested based on numerical calculations over a range of electron densities.

---

[f]The external potential term vanishes due to the neutrality of the gas.

In the Local-density approximation (LDA) the exchange correlation energy for the whole system is given by summing the uniform electron gas result over infinitesimal portions of a nonunifrom density.[g]

$$E_{xc}^{LDA}[\rho] = \int d\mathbf{r} \, \rho(\mathbf{r}) \epsilon_{xc}\left(\rho(\mathbf{r})\right) \tag{21}$$

where $\epsilon_{xc}(\rho(\mathbf{r}))$ is exchange-correlation energy per particle for a uniform electron gas of density ρ. This is easily extended to an unrestricted version for spin densities ρ_α and ρ_β,

$$E_{xc}^{LDA}[\rho_\alpha, \rho_\beta] = \int d\mathbf{r} \, \rho(\mathbf{r}) \epsilon\left(\rho_\alpha, \rho_\beta\right) \tag{22}$$

2.3.2 The Generalised Gradient Approximation

The local density approximation naturally works well for systems that approximate a uniform-electron gas, systems with slowly varying densities as often found in solid-state physics. However, it remains totally inadequate in modelling atoms, molecules and surfaces where large gradients exist in ρ. The logical step in extending the local density approximation to such cases is to include the gradient of the density. $\nabla \rho$ [h] This correction was first made by Becke in 1988 and was responsible for the general acceptance of density functional theory as a valuable tool in computational chemistry. Functionals of this kind are collectively known as generalised gradient approximations (GGA) and are generically written,[i]

$$E_{xc}^{GGA}[\rho] = \int d\mathbf{r} \, f(\rho, \nabla \rho) \tag{23}$$

A simple extension gives spin sensitive generalised gradient functionals (GGS),

$$E_{xc}^{GGS}[\rho_\alpha, \rho_\beta] = \int d\mathbf{r} \, f(\rho_\alpha, \rho_\beta, \nabla \rho_\alpha, \nabla \rho_\beta) \tag{24}$$

The physics underlying the phenomenal success of these functionals remains as mysterious as the form of the exact exchange-correlation functional. The use of these functionals remain solely justified *a posteriori* by their success.

---

[g]Note $\epsilon(\rho(\mathbf{r}))$ and $\epsilon(\rho_\alpha(\mathbf{r}), \rho_\beta(\mathbf{r}))$ are both are functions, rather than functionals, of ρ.

[h]Including $\nabla \rho$ in the functional can be viewed as introducing higher order terms into a Taylor expansion of the density ρ.

[i]More specifically, GGA functionals are those functionals containing $\nabla \rho$ which also impose certain constraints on the form of the exchange-correlation hole.

2.4   The meaning of the Kohn-Sham orbitals and eigenvalues

One-electron eigenstates and eigenvalues were introduced by Kohn and Sham solely as a theoretical construct required to solve the many-body problem. From equation 19 it is evident that for weakly correlated materials, where the coulomb and exchange-correlation energies are small, the Kohn-Sham eigenvalues ϵ_i are a good approximation to the single-particle terms. It can also be shown that, given an exact E_{xc}, the energy of the highest occupied eigenstate ϵ_{max} is exactly the negative of the ionisation energy. However, until recently no physical significance was attached to the Kohn-Sham orbitals beyond the fact that $\sum_i |\psi_i|^2 = \rho$. Lately however, the interpretative power of these orbitals has been used in rationalising chemical phenomena (14). This is justified by noting that because the Kohn-Sham orbitals return the exact ground state density and fully incoroporate all non-classical effects they are, in some sense, *more* physical than the Hartree-Fock orbitals of regular quantum chemistry. Although the single particle Kohn-Sham orbitals may used in qualitative molecular-orbital considerations, the true many-electron wave function remains unattainable in density-functional theory.

3   Implementing Density-functional theory

The success of density functional theory in first-principle simulation is largely attributable to the phenomenal computational efficiency achievable in its implementation. One such method, the plane-wave pseudopotential method (PWP) (15), stands high above other *ab initio* techniques in terms of the complexity of systems that can be handled. The PWP method functions within the Born-Oppenheimer approximation and further relies upon,

- *Pseudopotentials* to model electron-ion interactions

- *Iterative minimisation* to find the ground state

- *Supercells* to model aperiodic systems

- *Plane waves* as a basis set

Iterative methods are used to find the ground state, replacing the conventional matrix diagonalisation of traditional self-consistent field quantum chemistry. This

is because the cost of matrix diagonalisation scales as the third power of the number of plane-wave basis states, the memory requirement increases as the square [j] and all electronic-state eigenvalues are calculated even though the total energy depends only on the lowest occupied states. Furthermore, considerable effort is invested in computing the eigenvalues to great accuracy, even when the system is far from self-consistency. Iterative methods can avoid many of these costs by instead optimising the parameters of a solution to reach a minimum. Since the Kohn-Sham equations obey the variational principle the end result should be independent of the technique used to get there, provided the iterative method finds the global minimum.

3.1 Plane wave basis set

A plane wave basis set is the natural choice to describe the wave functions of solid state systems. Imposing Born-van-Karmen boundary conditions on an infinite extent of bulk material allows the wave functions to be decomposed into the Bloch form (16),

$$\psi_{n,\mathbf{k}}(\mathbf{r}) = u_{n,\mathbf{k}}(\mathbf{r}).e^{\mathbf{ik.r}} \tag{25}$$

where $u_{n,\mathbf{k}}(\mathbf{r} + \mathbf{R}) = u_{n,\mathbf{k}}(\mathbf{r})$ for any lattice vector $\mathbf{R}$. Different solutions are indexed by n at a fixed wave vector $\mathbf{k}$ which is chosen to lie in the first Brillouin zone. The cell-periodic part $u_{n,\mathbf{k}}(\mathbf{r})$ can be expanded using a discrete set of plane waves whose wave vectors are reciprocal lattice vectors of the crystal,

$$u_{n,\mathbf{k}}(\mathbf{r}) = \sum_{\mathbf{G}} \tilde{u}_{\mathbf{G}}^n e^{\mathbf{iG.r}} \tag{26}$$

where $\mathbf{G}$ are defined by $\mathbf{G.R} = 2\pi m$ for any integer m. Therefore, each electronic wave function is written as

$$\psi_{n,\mathbf{k}}(\mathbf{r}) = \sum_{\mathbf{G}} \tilde{u}_{\mathbf{G}}^n e^{\mathbf{i(k+G).r}} \tag{27}$$

Substituting for $\psi_n(\mathbf{r})$ into the Kohn-Sham equations (17) and integrating over $\mathbf{r}$ gives the secular equations,

$$\sum_{\mathbf{G'}} \left[\frac{\hbar^2}{2m} \left(\mathbf{k} + \mathbf{G} \right)^2 \delta_{\mathbf{GG'}} + \tilde{v}_{eff,(\mathbf{G}-\mathbf{G'})} \right] \tilde{u}_{\mathbf{k+G}}^n = \epsilon_n \tilde{u}_{\mathbf{k+G'}}^n \tag{28}$$

[j]Furthermore, roughly 100 plane waves per atom are required for the calculation.

where $\tilde{v}_{eff,\mathbf{G}}$ are the Fourier components of v_{eff} expanded over reciprocal lattice vectors, $v_{eff} = \sum_{\mathbf{G}} \tilde{v}_{eff,\mathbf{G}}.e^{i\mathbf{G}.\mathbf{r}}$. Solution of the secular equations are by diagonalisation of the Hamiltonian matrix whose elements $H_{\mathbf{k}+\mathbf{G},\mathbf{k}+\mathbf{G}'}$ are contained within the square brackets of equation 28. The size of this matrix and the accuracy of the plane wave expansion of $\psi_{n,\mathbf{k}}(\mathbf{r})$ is determined by the cutoff energy $E_c = \frac{\hbar^2}{2m}(\mathbf{k}+\mathbf{G}_c)^2$ where $\mathbf{G_c}$ is the wave vector at which the Fourier expansion of equation 27 is terminated in practical calculations. Larger cutoff energies allow more accurate calculations but are significantly more expensive because the number of $\mathbf{G}$ vectors smaller than $\mathbf{G}_c$ scales as $E_c{}^3$. Generally it is found that good convergence of the electronic structure requires higher cutoff energies than needed for the convergence of the total energy and lattice constants.

3.2   Supercells

An ideal surface is the plane between an infinite extent of bulk material and an infinite region of vacuum and so periodicity is lost in a direction normal to the surface ($R_\perp \rightarrow \infty$). Therefore the Bloch expansion (equation 25) becomes continuous ($G_\perp \rightarrow 0$) and two concessions must be made to allow practical calculations. Firstly, the system is made finite by using only a thin crystal slab. Secondly, periodic boundary conditions are reintroduced by constructing supercells which are repeated over all space. Each supercell contains a crystal slab and a vacuum region (figure 5). Both the slab and the vacuum must be sufficiently deep to prevent significant interaction between the two surfaces.

Ideally, the two surfaces of the slab are both relaxed about the middle section of the supercell which is held fixed in bulk geometry. This means that any deviations in the electronic structure from the bulk can be confidently assigned to the surfaces. However this approach is expensive and, where the two opposite surfaces are identical, wasteful since the same thing is computed twice. The alternative is to just relax one surface and freeze the other in bulk geometry. This is less computationally demanding but the effects of the unphysical back-surface must be corrected for when interpreting the electronic structure.
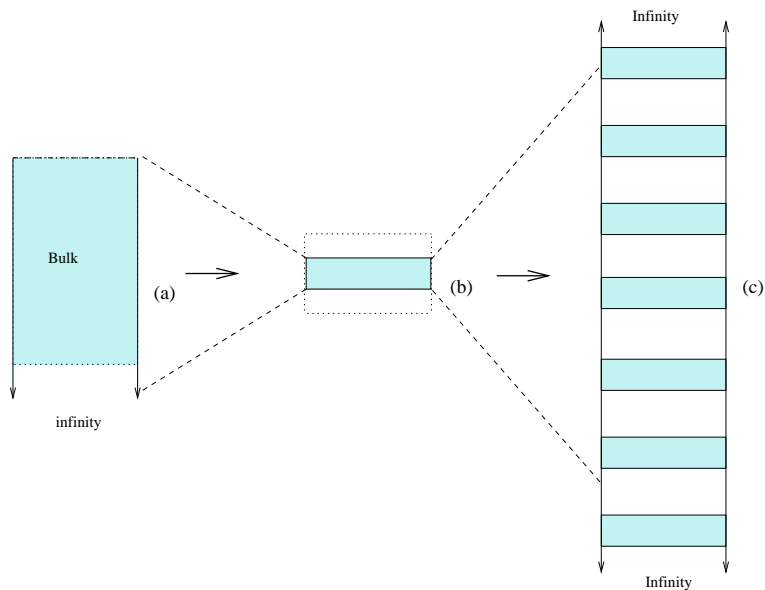
Figure 5: *Schematic illustration of the approximations necessary in modelling surfaces.*(a)Ideal surface; (b)Supercell containing finite crystal slab; (c)Periodic repetition of supercell over all space

3.3   Pseudopotentials

The pseudopotential approximation exploits the fact most physical properties depend predominantly on the valence electrons only. Even then, the component of the valence wave function near the nucleus has very little effect on the bonding properties of the valence electron. Within a radius r_c of the ion core, the correct potential v_{eff} is replaced by an new potential which combines the charge of the nucleus and core electrons and the real wave functions are replaced by pseudo wave functions. At r_c the pseudopotential becomes identical with the real potential and the pseudo-wave function (and its derivative) match the real the wave function.

By incorporating the core electrons into this new potential, wave functions for fewer electrons have to be calculated. There is also a large reduction in cost of representing valence wave functions near the nucleus. Representation in this region is normally expensive because the wave functions necessarily have large curvature to compensate for the large negative potential [k] and their form is further complicated by the requirement of orthogonality with the core states. However, orthogonality is no longer an issue within the pseudopotential model because there are no core electrons. The curvature can be minimised by choosing a weak potential (figure 6).

---

[k]For a stationary state, a decrease in the potential must be compensated for by an increase in the kinetic energy, therefore requiring a greater curvature of the wave function.
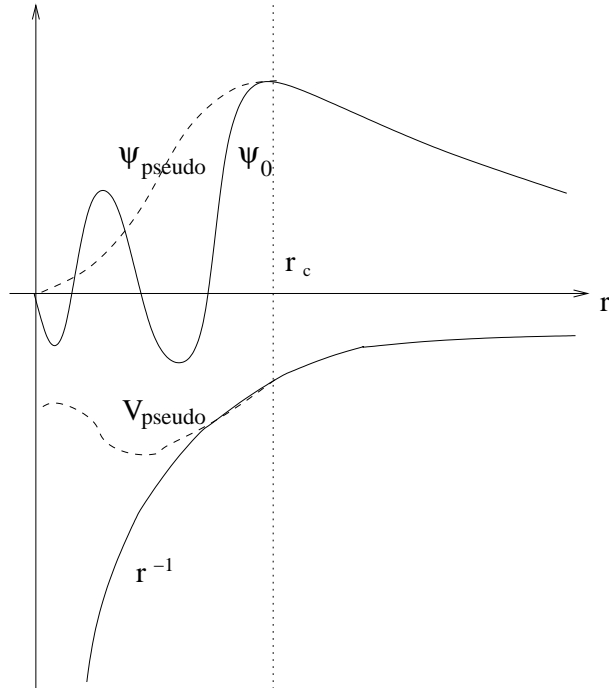
Figure 6: Schematic illustration of the potentials and wave functions for all-electron (solid lines) and pseudopotential (dashed lines) calculations. The radius at which wave functions (and their derivatives) match is denoted r_c

An accurate pseudopotential will not affect the form of the wave function beyond r_c and will reproduce the same energy of the core E_{core} as calculated by an all electron treatment. The exact shape of the pseudopotential can be adjusted to give the correct core energy E_{core}. To ensure that the pseudo and real wave functions match outside the core region, it is necessary and sufficient to adjust the pseudopotential so that

$$\int_0^{r_c} d\mathbf{r} \, |\psi_{exact}|^2 = \int_0^{r_c} d\mathbf{r} \, |\psi_{pseudo}|^2 \tag{29}$$

Pseudopotentials constructed according to this 'norm-conservation' criterion greatly reduce the computational cost in many cases. However, calculations remain expensive for atoms with tightly bound valence orbitals which have a substantial weight within the core region. This is the case for example, for the first row elements and transition metals. As a result even pseudo wave functions remain highly curved and are therefore expensive to represent, requiring a large cutoff energy. However, as suggested by Vanderbilt (17) in 1990, relaxing the norm-conservation condition allows a less highly localised and therefore cheaper function (figure 7). Corrections for this deviation from norm-conservation have to be made at a later stage in the

calculation. Such 'ultrasoft' potentials are now widespread in their application and alongside the relentless growth of computational power have greatly increased the size of calculation now possible.
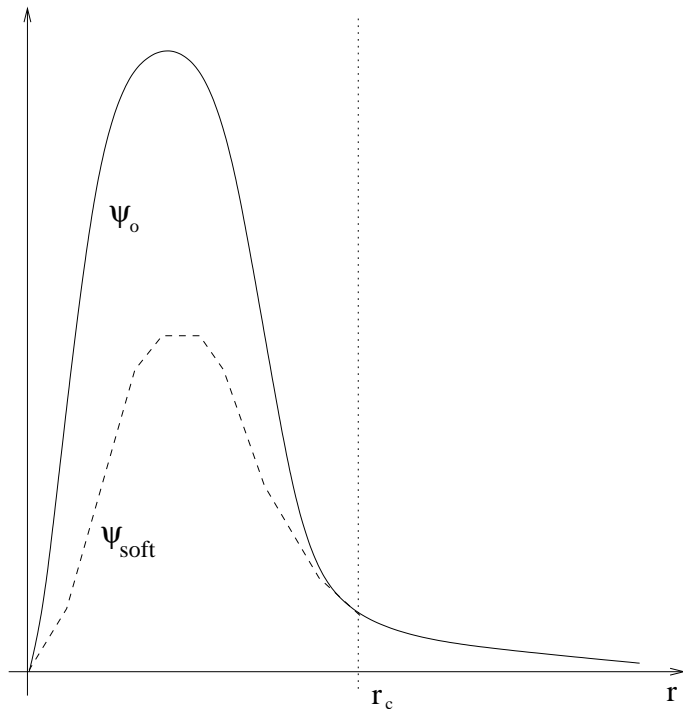

Figure 7: Two pseudo wave functions for a valence state highly peaked in the core; norm-conserving (bold) and ultrasoft (dashed)

The treatment above transfers all interactions between core and valence electrons to a local pseudopotential v_{pseudo} and the contribution to the total energy from the core region is given by,

$$E_{core} = \int d\mathbf{r} \, v_{pseudo}(\mathbf{r})\rho(\mathbf{r}) \tag{30}$$

However, unlike the Kohn-Sham effective potential v_{eff}, the pseudopotential v_{pseudo} does contain any dependence on the valence charge density ρ. Therefore the assumption implicit in equation 30 is that the energy of interaction between core and valence states is linear in ρ. This introduces no serious errors provided the valence and core charge densities are well separated in space. However, where there is significant overlap between the two densities the linearisation, in particular of the exchange-correlation energy, leads to large systematic errors. In such cases, non-linear core corrections must be incorporated into the core energy (18) $E_{core}^{core \; corrections}$ by treating v_{pseudo} as a function of ρ,

$$E_{core}^{core \; corrections} = \int d\mathbf{r} \, v_{pseudo}\left((\mathbf{r}), \rho(\mathbf{r})\right) \rho(\mathbf{r}) \tag{31}$$

These core corrections allow the behaviour of the core to adjust to the form of the valence wave functions and this improves the transferability of the pseudopotential over a range of chemical environments.

3.4   Sampling the Brillouin-zone

In theory, to determine the total energy of a system, all occupied states must be included. This would involve an integration over the Brillouin-zone and would be an unfeasibly large calculation. However, for large systems where $\mathbf{k}$ is quasi-continuous, the wave functions at proximate $\mathbf{k}$-points are almost identical. Therefore it is possible to represent wave functions over a region of $\mathbf{k}$-space by the function at a single $\mathbf{k}$-point. It was shown by Monkhorst and Pack (19) that the most efficient distribution of $\mathbf{k}$ for sampling are given by

$$\mathbf{k_j} = x_{1j}\mathbf{b_1} + x_{2j}\mathbf{b_2} + x_{3j}\mathbf{b_3} \tag{32}$$

where $\mathbf{b_i}$ are reciprocal lattice vectors and

$$x_{ij} = \frac{l_i}{n_j} \tag{33}$$

where l_i are the lengths of $\mathbf{b_i}$ and n_j is an integer determining the number of k-points in the set. This array of k-points may be further reduced in size by exploiting the point group symmetry of the Brillouin-zone and the sampling integral of a function $F(\mathbf{k})$ is replaced by the sum,

$$\sigma_{j=1}^{P(n_j)}\omega_j F(\mathbf{k_j}) \tag{34}$$

where $P(n_j)$ are the symmetry dependent k-points within the irreducible wedge of the Brillouin-zone and ω_j are the ratios of the order of the point group of the wave vectors $\mathbf{k_j}$, to that of the full point group symmetry.

3.5   The CASTEP code

In all the following, the CASTEP 4.2 (20) implementation of the plane wave pseudopotential approach is used. Fast Fourier transforms are used to interconvert between real and reciprocal space. Minimisation is by a conjugate-gradient method and electron-electron interactions are modelled with Perdew-Wang-91 functionals. Atoms are relaxed according to the Hellman-Feynmann theory.

Part III

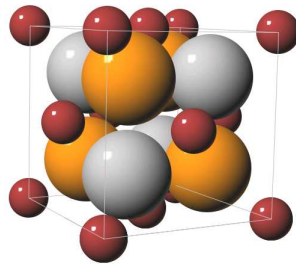# Bulk Calculations

4   Nickel Manganese Antimonide

Figure 8: NiMnSb conventional unit cell - an *fcc* lattice with basis Ni:(0,0,0), Mn:$(\frac{1}{4},\frac{1}{4},\frac{1}{4})$ and Sb:$(\frac{3}{4},\frac{3}{4},\frac{3}{4})$

NiMnSb crystallises in the $C1_b$ structure and was modelled using the primitive *fcc* unit cell and GGS functionals. Electronic wavefunctions were expanded up to a kinetic energy cutoff of 300 eV and a Monkhorst-Pack mesh of 4 x 4 x 4 was used. Ultrasoft pseudopotentials where used for all atoms and non-linear core corrections were applied to Ni and Mn. Such treatment returns a conventional lattice constant of 5.89 Å, within 1% of the experimental value of 5.97 Å. (5) The determination of the electronic structure also agrees well with previous theoretical work. (1; 21) The magnetic moment is calculated to be 4.00 μ_B per primitive unit cell [1] and the band structure displays huge asymmetry between spin states, with an indirect band gap of 0.54 eV for minority spin states and Fermi level crossing for majority spin states (figure 10). For interest, the projection of the band structure along [**100**] between high symmetry points in the surface Brillouin zone is also shown.

5   Indium Phosphide

Indium Phosphide crystallises in the zinc-blende structure and was modelled in the primitive unit cell, sampled by a 6 x 6 x 6 k-point mesh. The $4d$ states were considered as valence electrons for In and ultrasoft pseudopotentials were used throughout.

---

[1]An integer magnetic moment is a property of all half-metals, arising from the fact that all minority spin bands lie wholly below the Fermi level.
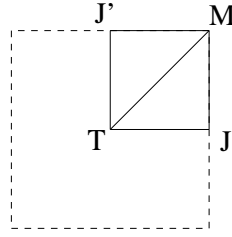
Figure 9: The surface Brillouin zone of an *fcc* lattice and its high symmetry points
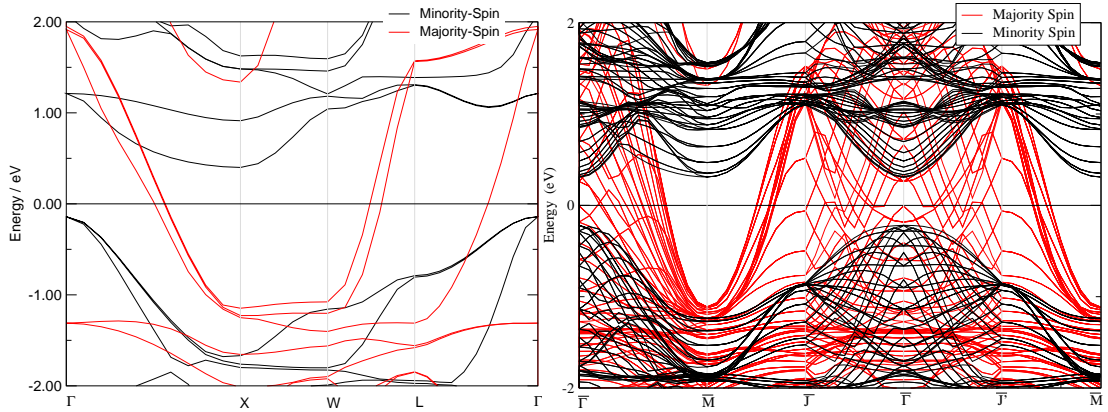

Figure 10: NiMnSb majority and minority spin band structures (left) and their projections along $\langle\mathbf{100}\rangle$ (right) for a (1x1) surface mesh. **k**-space is traversed between high symmetry points $\Gamma = (0, 0, 0)$; $X = (0, 0, 0)$; $W = (-\frac{1}{4}, \frac{1}{2}, \frac{1}{4})$; $L = (0, \frac{1}{2}, 0)$

The plane wave expansion of electronic wave functions was up to a kinetic energy cutoff of 310 eV. The lattice constant was accurately determined as 5.93 Å, within 1% of the experimental value of 5.87 Å (22). The form of the band structure is that
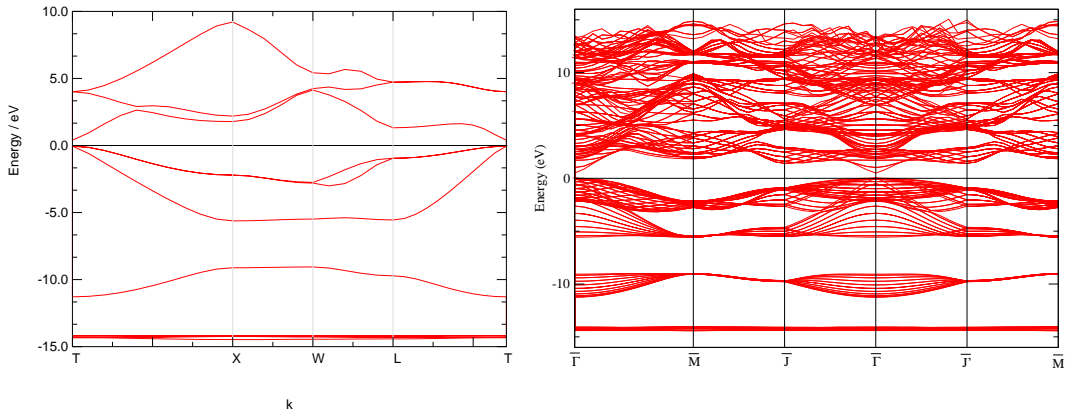

Figure 11: The band structure of InP (left) and its projection along $\langle\mathbf{100}\rangle$ (right) for a (1x1) surface mesh. **k**-space is traversed between high symmetry points $\Gamma = (0, 0, 0)$; $X = (0, 0, 0)$; $W = (-\frac{1}{4}, \frac{1}{2}, \frac{1}{4})$; $L = (0, \frac{1}{2}, 0)$

expected for a zincblende unit cell and generally matches experimental results (23). However, the calculated band structure shows a direct band gap of only 0.47 eV in comparison with the experimental value of 1.27 eV (22). Poor representation

of band gaps is a common feature of density-functional theory which is strictly a ground state method only. [m] However, our underestimate of the band gap is particularly large compared with previous studies (24) and is attributed to our use of the theoretically most favourable lattice parameter instead of the experimental value (figure 12).
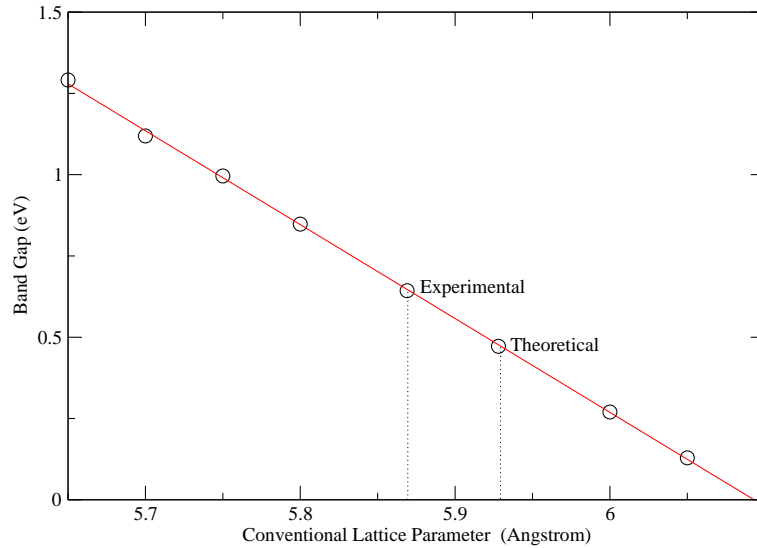

Figure 12: Change in calculated band gap with lattice parameter used in calculation. The increase in band gap with compression of the unit cell is the behaviour expected from increased confinement of electrons.

---

[m]This inaccuracy of DFT stems from an overestimation of the amount of screening experienced by electrons in the conduction bands (by using a E_{xc} which is fixed). In a metal, where there are continuous bands at the Fermi level, there is a lot of screening and so this error is minimal. However, the excited states of an insulator have minimal screening and so the error becomes very apparent.

Part IV

InP Surface Calculations

As discussed in section 3.2, an accurate model of the surface largely depends upon the choice of appropriate supercell dimensions. However the InP {100} surfaces which are terminated exclusively by either In or P, pose additional problems. For a supercell slab terminated by one In surface and one P surface, electrons unavoidably flow toward the more electronegative P surface. This 'charge sloshing' effect introduces an artificial electric field into the model which has unphysical effects on the surfaces.
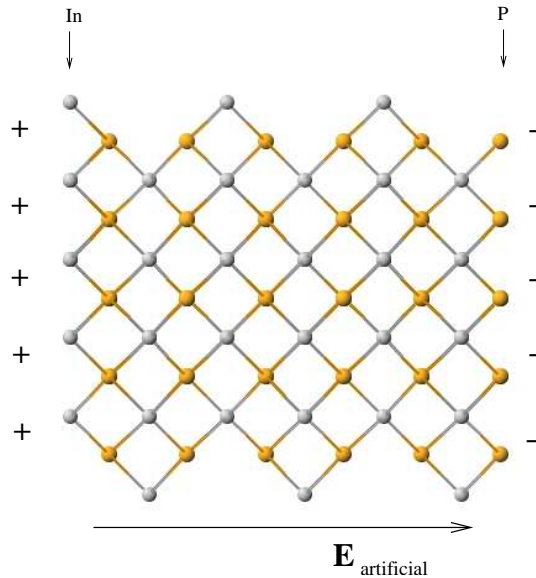

Figure 13: The artificial electric field resulting from charge transfer between two InP{100} surfaces of opposite polarity.

The asymmetry between the surfaces, and the necessarily finite sized supercell slab, introduces a further problem. Each surface will have its own surface states and associated Fermi-level. Within a calculation, the Fermi-level will try to equalise across the whole structure and in doing so will bend the bulk bands. This coupling between non-identical surface states is called Fermi-level pinning and is another substantial non-physical effect that must be accounted for.

One very elegant method simultaneously reduces the effect of both of these complications. The top surface of the slab is left to relax in the normal manner and the back surface is adjusted to behave like an infinite extent of bulk material, so min-

imising any unphysical effects. This technique of 'back surface termination' most commonly uses fractionally charged hydrogens to form perfect covalent bonds with the surface. In doing so, partially-occupied dangling surface states are replaced with fully occupied bonding orbitals and thus charge-sloshing is prevented. Furthermore, the bonding and anti-bonding orbitals are energetically removed from the original surface state and so coupling to the opposite surface is greatly reduced. [n] Unfortunately the CASTEP 4.2 code we use is unable to handle fractional charges, and so an alternative back surface termination must be developed.

In light of the subtleties involved in modelling InP {100}, we first model the {110} surface to verify the accuracy of our methodology. The {110} surface of InP forms identical surfaces on each side of the supercell slab and so there are no issues with charge sloshing and Fermi level pinning.

6   The InP {110} Surface

The stable InP{110} (1x1) reconstruction is modelled in a supercell of height 22.8 Å containing six atomic InP{110} layers and a 12.1 Å region of vacuum. The calculation is found to be converged for these supercell dimensions. The experimental lattice constant of 5.87 Å is used and GGA functionals are employed to model electron-electron interactions. $\mathbf{k}$-space integrations are replaced by a sum over ten special points in the irreducible part of the surface Brillouin zone and single-particle orbitals are expanded into plane waves up to a cutoff of 310 eV. The back surface is frozen in bulk geometry and the top three atomic layers are allowed to relax.

At the surface P is found to move out from, and In towards, the bulk (figure 14). The In-P bondlength at the surface is found to be contracted by 1% relative to the bulk value, in good agreement with LEED experiments (25). The buckling angle is found to be 27.3° compared with a previous theoretical prediction of 26.5° (26).

---

[n]Another technique is to terminate both surfaces identically - this is very expensive computationally since symmetry must be conserved to prevent Fermi-level pinning and so both surfaces must be relaxed.
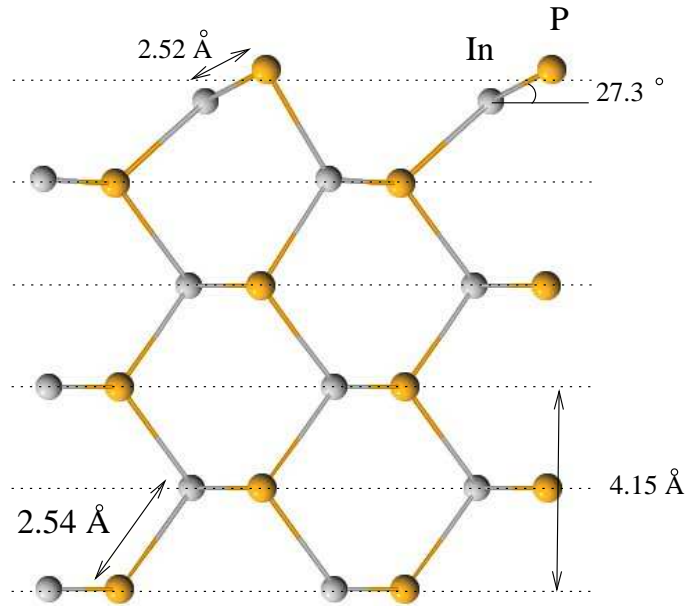
Figure 14: Side view of the InP {110} reconstruction. Yellow (grey) circles represent P (In) atoms

7 The InP {100} Surface

The InP{100} surface displays a rich and varied chemistry that depends upon the conditions under which it is made (27). Previous theoretical studies have presented a comprehensive study of this surface (28; 29; 30) by comparing the stability of several structural models of the {100} reconstructions. In comparing the favourability of different reconstructions it is necessary to refer to the free energy of the surface.

7.1 Surface Thermodynamics

The total energy returned by a calculation depends on the number of atoms in the supercell. Since this number varies with the reconstruction being modelled it is necessary to remove this dependence in order to compare the energy of reconstruction. We therefore construct a free energy F_{InP},

$$F_{InP} = E_{InP} - n_{In}\mu_{In} - n_P\mu_P \tag{35}$$

where n_x is the number of atoms with chemical potential μ_x and E_{InP} is the calculated total energy. However, μ_{In} and μ_P depend on the prevailing chemical environment and remain unknown. Nonetheless it must be that

$$\mu_x \leq \mu_x^{bulk} \tag{36}$$

where μ_x^{bulk} is the chemical potential of bulk x. Furthermore μ_{In} and μ_P must be related to each other by

$$\mu_{In} + \mu_P = \mu_{InP}^{slab} \tag{37}$$

where μ_{InP}^{slab} is the chemical potential of the supercell slab. We assume that within the slab bulk behaviour dominates any surface effects, and so we may write $\mu_{InP}^{slab} = \mu_{InP}^{bulk}$ where μ_{InP}^{bulk} is simply the total energy for a bulk primitive unit cell calculation. Equation 35 can now be written as the function of a single variable which we take as μ_{In}

$$F_{InP} = E_{InP}^{Total} - (n_{In} - n_P)\,\mu_{In} - n_P \mu_{InP}^{bulk} \tag{38}$$

for which the boundary conditions are now

$$\mu_{InP}^{bulk} - \mu_P^{bulk} \leq \mu_{In} \leq \mu_{In}^{bulk} \tag{39}$$

or alternatively

$$\Delta_f H(InP) \leq \Delta\mu_{In} \leq 0 \tag{40}$$

where $\Delta\mu_{In} = \mu_{In} - \mu_{In}^{bulk}$ and $\Delta_f H(InP)$ is the heat of formation of InP.

7.2 (2x4) reconstructions of InP{100}

In 1998 Schmidt and Bechstedt (28; 29) proposed eleven (2x4) reconstructions for the InP{100} surface and used density-functional theory in the local-density approximation to calculate the favourability of these reconstructions over the full range of allowed chemical potentials (graph 15). In the following we attempt to reproduce and expand upon these results for the four most stable, P terminated, (2x4) reconstructions (shown in figure 18).

There are two main differences between our approach and that of Schmidt and Bechstedt (hereafter referred to as SB). Firstly SB use fractionally charged hydrogens (Z=1.25) to terminate an In surface whereas we must introduce a novel back-surface design to overcome the inability of the CASTEP code to handle fractional charges (see section 7.2.2). Secondly, SB, whose work dates from 1998, followed the common practice of their time and treated the $4d$-states of In as frozen core states within the pseudopotential so as to reduce the computational cost of calculation.
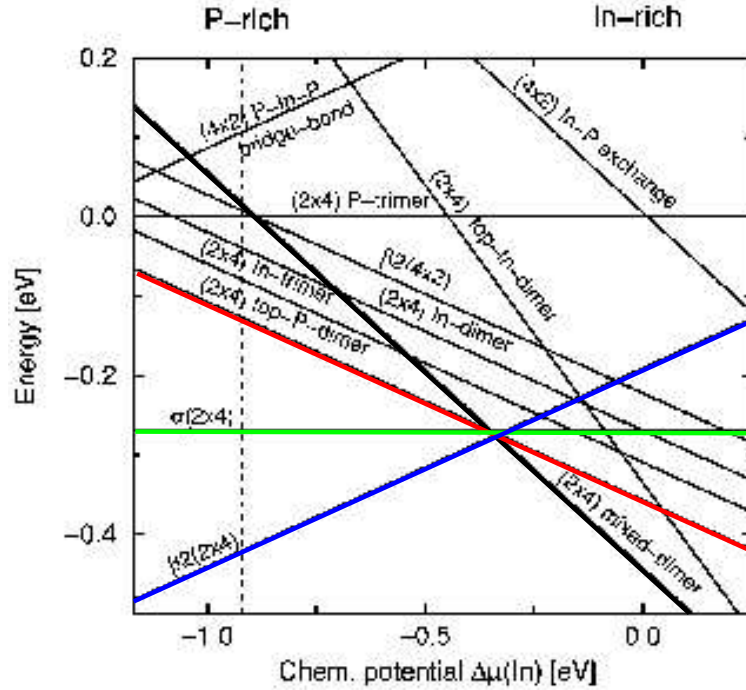
Figure 15: *The work of Schmidt and Bechstedt.* Free energies of (2x4) reconstructions against $\Delta\mu_{In}$. The four highlighted lines indicate the reconstruction models we chose to study; Black: mixed-dimer; Red: top-P-dimer; Green: α; Blue: β_2.

On the other hand the CASTEP 4.2 pseudopotential for In does not include the $4d$-electrons but treats In as having 13 valence electrons. We perform calculations using this more complete description of In (hereafter referred to as *In-(13)*) and also repeat the calculations using a treatment similar to that of SB, with only 3 In valence electrons (hereafter referred to as *In-(3)*). We show that the more accurate 13 electron description has only marginal effects on the results obtained.

7.2.1 Calculation parameters

Our density-functional calculations employ the generalised gradient approximation. We model the (2x4) reconstructions using a supercell containing six atomic InP{100} layers, a three layer back surface termination (discussed below) and a 6.5 Å region of vacuum. We allow the top four atomic layers to relax whilst keeping frozen two of the back InP{100} layers and most of the back surface (see below). Ultrasoft pseudopotentials were employed throughout but very high energy cutoffs were used nonetheless to allow comparison with future work on the electronic structure (section 3.1). The *In-(3)* pseudopotential was constructed using the USPP code (31) and included non-linear core corrections (section 3.3). It was found to behave well

in models of bulk In and InP. A cutoff of 300 eV was used for this pseudopotential whilst the *In-(13)* pseudopotential required a cutoff of 310 eV. Only one special **k**-point was used in sampling the Brillouin zone, corresponding to a Monkhorst-Pack mesh of 2 x 1 x 1. The theoretical equilibrium bulk lattice constant of InP is found to vary little with the pseudopotential used, and we use the *In-(13)* value of 5.93 Å in all calculations.

7.2.2 Back-surface termination

We propose a new termination for the back In surface of our slab. For an ideal back surface termination the relaxed top layer of the supercell slab would feel as though surrounded by perfect bulk material on one side and vacuum on the other. To achieve this, the back In surface must somehow be in a bulk-like state with a full compliment of electrons. Bulk In atoms are four-fold coordinated and are five electrons short of noble-gas electron configuration. Therefore, to achieve a closed-shell configuration each In atom must gain 1.25 electrons per bond made. Thus, on the In surface, we first form a layer consisting of equal quantities of Si and P, then a layer of just Si and finally a layer of H atoms. All atoms are held in the zincblende configuration except for the H which are relaxed. Allowing movement of the H helps the back surface respond to small changes on the relaxed surface in the same way that an infinite extent of bulk would. Every atom (except the H) forms four two-electron bonds so the electron contribution to each bond from each atom is

- Indium:- 0.75 electrons to four bonds

- Phosphorous:- 1.25 electrons to four bonds

- Inner Silicon:- 1.25 electrons to two bonds, 0.75 electrons to two bonds

- Outer Silicon:- 1.25 electrons to one bond, 0.75 electrons to one bond, 1.0 electrons to two bonds

- Hydrogen:- 1.0 electrons to one bond

To determine the accuracy of our termination, we compare slabs of differing thickness which are terminated on both sides (see figure 17). The two calculations
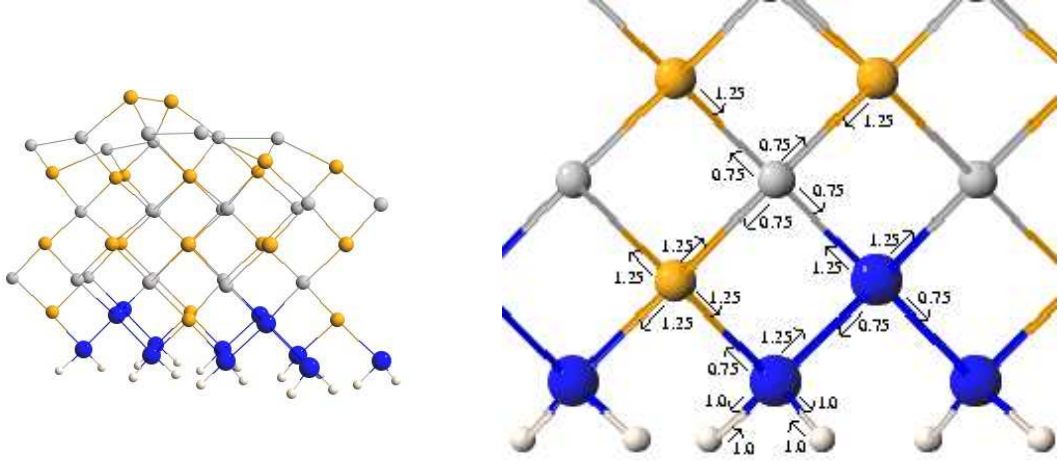
Figure 16: Our novel termination of the In back-surface and the contributions to two-electron bonds. P atoms are coloured yellow, In atoms grey, Si atoms blue and H atoms white

differ only in the insertion of an extra InP{100} layer into the larger slab, corresponding to an extra four InP units. The supercell is 20.7 Å in height for both slabs and the vacuum region has a height of 7.0 Å and 10 Å for large and small slabs respectively. The *In-(13)* pseudopotential is used and all other calculation parameters are as discussed above. It is found that the difference in total energy ΔE is almost identical to four times the chemical potential of bulk InP μ_{InP}^{bulk} (table 1) where μ_{InP}^{bulk} is taken to be -1747.2 eV (section 7.2.3). This means that the extra layer in the large supercell is essentially in a bulk environment and therefore our termination must accurately mimic an infinite extent of bulk. Furthermore, for ΔE to be linear in μ_{InP} must mean there is negligible interaction between the two surfaces and we may therefore conclude the Fermi-level pinning effects are successfully removed. On this ground, and the assumption that charge-sloshing is minimal, we use this termination and continue with our calculations.
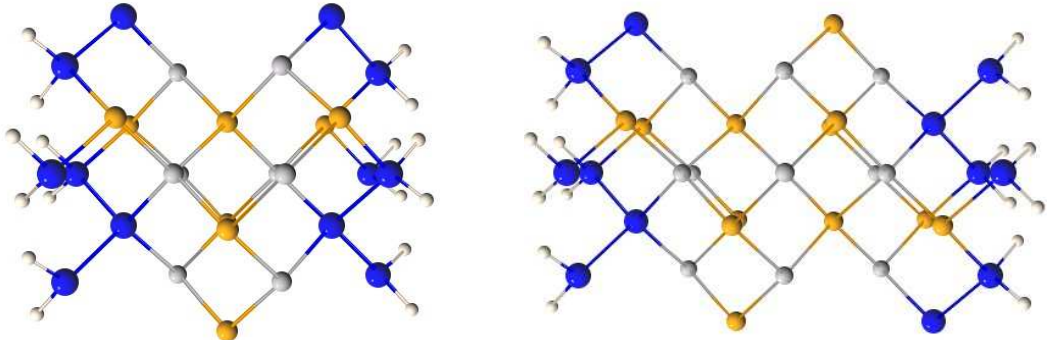

Figure 17: Small and large doubly terminated slabs used to estimate effectiveness of back surface termination.

	Total Energy E (eV)	ΔE	$4.(\mu_{InP})$
Small Slab	-15529.6		
		-6989.3	-6988.8
Large Slab	-22518.9		

Table 1: The difference in total energy calculations for small and large slabs compared with energy of insertion of 4 InP units.

7.2.3 The chemical potential range

As discussed in section 7.1 we can only compare the stability of surface reconstructions by considering their free-energies. Following the workings of this section we need to determine the upper and lower bounds of the chemical potential of In (equations 39 and 40). Since the use of pseudopotentials does not allow absolute treatment of energies (section 3.3) these boundary conditions must be computed for both the In-(13) and In-(3) pseudopotentials individually.

The calculated chemical potentials and the details of their derivation are shown in table 2. The total energy calculation for In and InP primitive unit cells gives μ_{In}^{bulk} and μ_{InP}^{bulk} but the calculation of μ_P^{bulk} is non-trivial due to the many amorphous and crystalline forms of phosphorus. The most stable allotrope is black phosphorus whilst the most common is white phosphorus. Due to the very large unit cells of other polymorphs, black phosphorus in its cubic form is chosen for calculations. However this approach yields

$$-0.4 \ eV \leq \Delta\mu_{In} \leq 0 \ eV \tag{41}$$

which is an unfeasibly small range of thermodynamically allowed values for a stable material such as InP. This small range corresponds to using a value of μ_P^{bulk} which is too small because P has been modelled in a structure which is too stable.

	Unit cell	Monkhurst-Pack mesh	μ (eV)
μ_{In}^{bulk}	primitive tetragonal $a = b = 3.25 \ \text{Å}, c = 4.95 \ \text{Å}$ (32)	5 x 5 x 3	-1565.9 (In-(13)) -399.6 (In-(3))
μ_{InP}^{bulk}	primitive zincblende $a = 5.93 \ \text{Å}$	6 x 6 x 6	-1747.2 (In-(13)) -580.9 (In-(3))
μ_P^{bulk}	Black-P primitive cubic $a = 2.38 \ \text{Å}$ (32)	8 x 8 x 8	-180.9

Table 2: The calculated chemical potentials of In, InP and P

However, although it is preferable to determine the upper and lower bounds on

$\Delta\mu_{In}$ using only first-principle results, it is possible to avoid the complications of working with μ_P^{bulk} by referring instead to the experimental heat of formation of InP $\Delta_f H(InP)$ as in equation 40.°. Taking $\Delta H_f(InP)$ = -0.92 eV (22) gives

$$-0.92\ eV \leq \Delta\mu_{In} \leq 0\ eV \tag{42}$$

or

$$-1566.8\ eV \leq \mu_{In} \leq -1565.9\ eV \tag{43}$$

for *In-(13)* and

$$-400.5\ eV \leq \mu_{In} \leq -399.6\ eV \tag{44}$$

for *In-(3)*.

7.2.4   Results

From the work of SB the four most stable surface reconstructions were chosen (figure 18). Crude estimates of these surface geometries were entered into our model (section 7.2.1) and equilibrium structures were found by the CASTEP 4.2 code. Calculations were run for both the *In-(13)* and *In-(3)* pseudopotentials and equilibrium geometries are shown in table 3.

To compare energies of surface reconstructions we follow the working of section 7.1 and use the free energy F_{InP},

$$F_{InP} = E_{InP} - \mu_{In}\left(n_{In} - n_P\right) - n_P\mu_{InP}^{bulk} \tag{45}$$

The values of F_{InP} over the allowed range of μ_{In} are shown in table 4 and plotted in graph 19.

Free energy plots for the two pseudopotentials agree well with those of SB (graph 15) as do our equilibrium geometries (table 3). Our results also show a certain $\Delta\mu_{In}$ where all four reconstructions become very similar in energy. The variation in $\Delta\mu_{In}$ at which this happens does not necessarily correspond to any substantial error since it is the coincidence of very shallow lines. It may seem strange that all


°$\Delta_f H(InP)$ is the enthalpy change from elements in their standard state, which for phosphorus is its white allotrope. From this state $\Delta_f H(Black - P) = -0.41\ eV$ and so we get the much more likely allowed range of $-0.81\ eV \leq \Delta\mu_{In} \leq 0\ eV$

| InP{001}-(2x4)	*In-(13)*	*In-(13)*	*Literature*
<u>*β₂*</u>			
P-P dimer (1st layer)	2.18	2.19	*2.21*
P-P dimer (3rd layer)	2.20	2.20	*2.25*
$d_{12} \perp$	1.53	1.53	*1.55*
<u>*α*</u>			
P-P dimer	-	2.18	*2.22*
$d_{12} \perp$	-	1.49	*1.44*
<u>Mixed-dimer</u>			
In-P dimer	2.60	2.61	*2.44*
Dimer buckling	0.37	0.35	*0.46*
$d_{12} \perp$	1.07	1.14	*1.08*
<u>Top-P-dimer</u>			
P-P dimer	2.18	2.18	*2.22*
$d_{12} \perp$	1.55	1.54	*1.50*

Table 3: *Equilibrium geometries (Å) of InP{100}(2x4) reconstructions.* Calculated for *In-(13)* and *In-(3)* and compared with the results of Schmidt and Bechstedt. The *In-(13)* calculation for the α reconstruction remains unfinished.

	Pseudopotential	E(eV)	μ_{In} (eV)	F(eV)
β₂	*In-(13)*	-5043.25	-1566.8	-194.25
			-1565.9	-194.025
	In-(3)	-1836.01	-400.5	-193.438
			-399.6	-193.213
α	*In-(13)*	-5434.75	-1566.8	-194.05
			-1565.9	-194.05
	In-(3)	-1935.98	-400.5	-193.275
			-399.6	-193.275
Mixed-dimer	*In-(13)*	-5562.63	-1566.8	-193.613
			-1565.9	-194.063
	In-(3)	-1918.04	-400.5	-192.925
			-399.6	-193.375
Top-P-dimer	*In-(13)*	-5389.49	-1566.8	-193.813
			-1565.9	-194.038
	In-(3)	-1890.68	-400.5	-193.075
			-399.6	-193.3

Table 4: Total and free energies of surface reconstructions for *In-(13)* and *In-(3)* pseudopotentials, normalised to (1x1) surface mesh
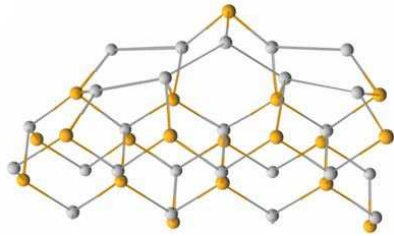
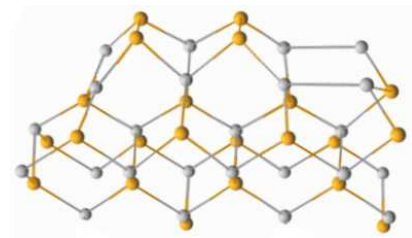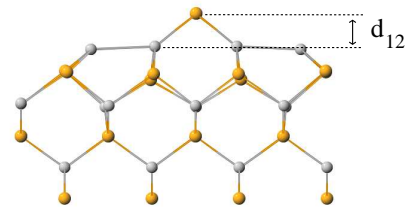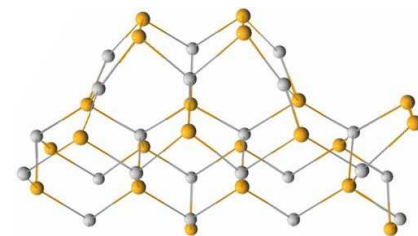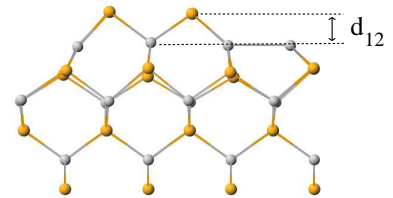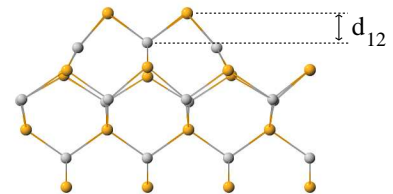(2x4) mixed–dimer

(2x4) top–P–dimer

α (2x4)
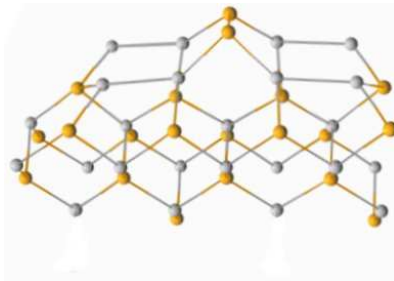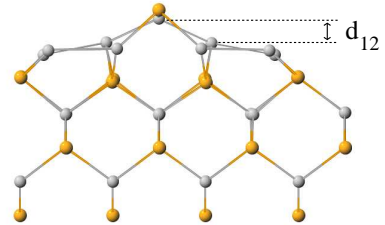
β $_2$ (2x4)

Figure 18: Side-top and top views of equilibrium geometry of InP{100}(2x4) reconstructions. Yellow (grey) circles represent P (In) atoms.
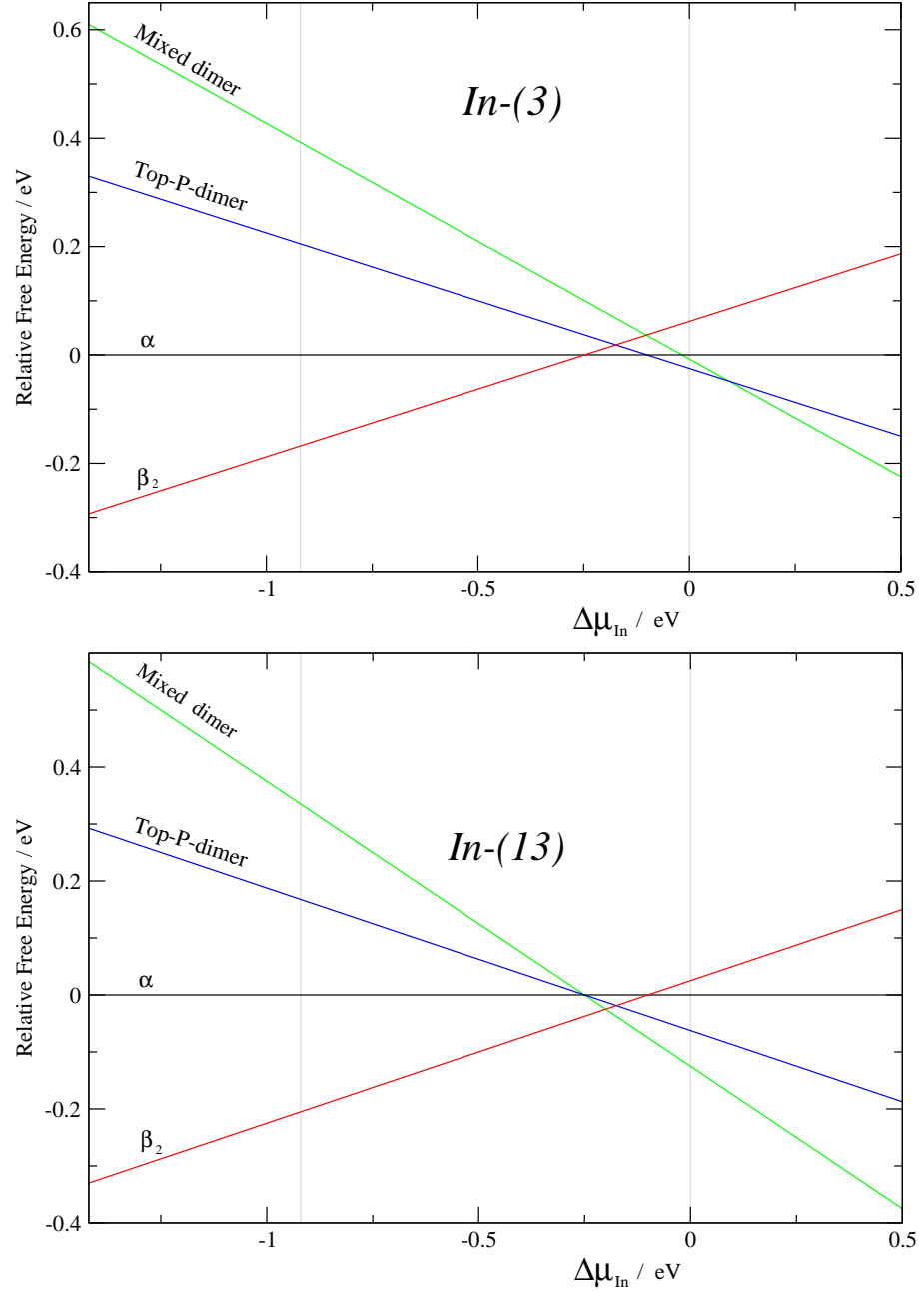
Figure 19: The relative free-energy of reconstruction (relative to α reconstruction) against $\Delta\mu_{In}$ for *In-(3)* and *In-(13)* pseudopotentials. The thermodynamically allowed range, $\Delta H_f(InP) \leq \Delta\mu_{In} \leq 0$, is indicated by grey lines.

these lines meet at a single point but in the context of many more reconstruction models (graph 15) this is likely to just be coincidental.

The similarity of the results from the *In-(3)* and *In-(3)* pseudopotentials suggest that only in the In-rich environment (large $\Delta\mu_{In}$), where the four reconstructions become comparable in energy, is it necessary to use the *In-(3)* pseudopotential. In the P-rich environment where the energy separation between structures is large, *In-(3)* could confidently be applied. This is of great computational use since it could greatly reduce computational cost in future calculations. However, this work does not exclude the possibility of other reconstruction structures that may complicate the behaviour of InP{100} in the P-rich environment.

Part V

Conclusion

A model has been developed for describing the InP{100} surface within the CASTEP implementation of density-functional theory. This approach is based on accurate calculations for bulk InP and NiMnSb and for the InP{110} surface. Applying this model to certain (2x4) reconstructions of the InP{100} surface reproduces well existing literature results. A novel back surface termination is demonstrated to be work. It is shown that neglecting the $4d$-electrons of In does not necessarily produce great errors and certain calculations could be performed with the cheaper 3 electron treatment of In.

Further theoretical work will involve modelling a greater range of InP{100} reconstructions and building NiMnSb{100} layers onto the most stable of these. Experimental work at Warwick aims to fabricate the NiMnSb / InP {100} interface by molecular beam epitaxy.

References

[1] R. A. de Groot and F. M. Mueller. New class of materials: Half-metallic ferromagnets. *Physical Review Letters*, 50(25), 1983.

[2] K. Schwarz. CrO_2 predicted as a half-metallic ferromagnet. *Journal of Physics F: Metal Physics*, 16:L211, 1986.

[3] R.A. de Groot, F.M. Mueller, P.G. van Engen, and K.H.J. Buschow. Half-metallic ferromagnets and their mangneto-optical properties. *Journal of Applied Physics*, 55:2151, 1984.

[4] E. Jouguelet J.F. Gregg, I. Petej and C. Dennis. Spin electronics - a review. *Journal of Physics D: Applied Physics*, 35:R121–R155, 2002.

[5] M.J. Otto, R.A.M. van Woerden, P.J. van der Valk, J. Wijngaard, C.F. van Bruggen, C. Haas, and K.H.J. Buschow. Half-metallic ferromagnets: I. structure and magnetic properties of NiMnSb and related inter-metallic compounds. *Journal of Physics of Condensed Matter*, 1:2341, 1989.

[6] I. Galanakis, S. Ostanin, M. Alouani, H. Dreysse, and J.M. Wills. *Ab Initio* ground state and $l_{2,3}$ x-ray magentic circular dichroism of Mn-based Heusler alloys. *Physics Review B*, 61:4093, 2000.

[7] R.B. Helmholdt, R.A de Groot, F.M Mueller, P.G. van Engen, and K.H.J. Buschow. Magnetic and crystallographic properties of several C_{1b} type Heusler compounds. *Journal of Magnetism and Magnetic Materials*, 43:249, 1984.

[8] D. Ristoiu, J.P. Nozieres, C.N. Borca, T. Komesu, H.K. Jeong, and P.A. Dowben. The surface composition and spin polarisation of NiMnSb epitaxial thin films. *Europhysics Letters*, 49:624, 2000.

[9] G.A. de Wijs and R.A. de Groot. Towards 100% spin-polarised charge-injection: The half-metallic NiMnSb/CdS interface. *Physical Review B*, 64:020402, 2001.

[10] W. Kohn P. Hohenberg. Inhomogeneous electron gas. *Physical Review*, 136:B864, 1964.

[11] W. Kohn and L.J. Sham. Self-consistent equations including exchange and corretaion effects. *Physical Review*, 140:1133, 1965.

[12] G.P Parr and W. Yang. *Density-functional Theory of Atoms and Molecules.* Oxford Science Publications, second edition.

[13] W. Koch and M.C. Holthausen. *A Chemist's Guide to Density-Functional Theory.* Wiley-VCH, second edition.

[14] R. Stowasser and R. Hoffmann. What do the Kohn-Sham orbitals and eigenvalues mean? *Journal of American Chemical Society*, 121:3414, 1999.

[15] M.D. Segall, P. Lindan, M. Probert, C. Pickard, P. Hassnip, S. Clark, and M. Payne. First-principles simulation: ideas, illustrations and the CASTEP code. *Journal of Physics of Condensed Matter*, 14:2717, 2002.

[16] Mermin Ashcroft. *Solid State Physics.* Brooks and Cole.

[17] D. Vanderbilt. Soft self-consistent pseudopotentials in a generalised eigenvalue formalism. *Physical Review B*, 41:7892, 1990.

[18] S.G. Louie. Nonlinear ionic pseudopotentials in spin-density-functional calculations. *Physical Review B*, 26:1738, 1981.

[19] H.J. Vanderbiltm J.D. Pack. Special points for Brillouin-zone integrations. *Physical Review B*, 13:5188, 1976.

[20] M. Payne, M. Teter, D. Allan, T. Arias, and J. Joannopoulos. Iterative minimization techniques for *ab initio* total-energy calculations: molecular dynamics an conjugate gradients. *Reviews of Modern Physics*, 64, (4):1045, 1992. CASTEP 4.2 academic version, licensed under the UKCP-MSI agreement, 1999.

[21] S.J. Jenkins and D.A. King. Minority metallic surface states of a half-metallic ferrimagnet. *Surface Science Letters*, 494:L793–L798, 2001.

[22] CRC Handbook of Chemical and Physical Constants, 84th edition.

[23] L. James, J. Van Dyke, F. Herman, and D. Chang. Band structure and high field transport properties of InP. *Physical Review B*, 1:3998, 1970.

[24] S.J. Jenkins. PhD thesis, University of Exeter, 1995.

[25] P.S. Mangat. Polarisation dependent photoemission EXPAS investigation of the InP {110} surface. *Surface Science*, 285:102, 1993.

[26] P. Ebert et al. The electronic structure of the InP(110) surface studied by scanning tunneling microscopy and spectroscopy. *Surface Science*, 271:587, 1992.

[27] W.G. Schmidt, J. Bernholc, and F. Bechstedt. (001) surfaces of GaP and InP: structural motifs, electronic states and optical signatures. *Applied Surface Science*, 166(179), 200.

[28] W. Schmidt and F. Bechstedt. Atomic structure of InP(001)-(2x4): A dimer reconstruction. *Physical Review B*, 57:14 596, 1998.

[29] W. Schmidt and F. Bechstedt. Geometry and electronic structure of InP(001)(2x4) reconstructions. *Surface Science*, 409:47schmidt4, 1998.

[30] O. Pulci, K. Ludge, P. Vogt, N. Esser, W. Schmidt, W. Richter, and F. Bechstedt. First-principles study of InP and GaP(001) surfaces. *Computational Materials Science*, 22:32, 2001.

[31] *Ultrasoft Pseudopotential code.*

   `http://www.physics.rutgers/edu/_dhb/uspp`

   . Open source code for construction of ultrasoft pseudopotentials.

[32] A. Earnshaw N. Greenwood. *Chemistry of the Elements*. Butterworth-Heinenmann, second edition.